OUKA
The University of Osaka
Institutional Knowledge Archive

Title	Magnetic penetration depth in topological superconductors: Effect of Majorana surface states and application for UTe_2
Author(s)	Akuzawa, Kazuki; Tei, Jushin; Ohashi, Ryoi et al.
Citation	Physical Review B. 2026, 113(14), p. 144506
Version Type	VoR
URL	https://hdl.handle.net/11094/104991
rights	Copyright (2026) by the American Physical Society
Note	

The University of Osaka Institutional Knowledge Archive : OUKA

https://ir.library.osaka-u.ac.jp/

The University of Osaka

Magnetic penetration depth in topological superconductors: Effect of Majorana surface states and application for UTe_2

Kazuki Akuzawa,[1] Jushin Tei,[1,*] Ryoi Ohashi,[2] Satoshi Fujimoto,[1,3,4,†] and Takeshi Mizushima[1,‡]

[1]*Department of Materials Engineering Science, The University of Osaka, Toyonaka 560-8531, Japan*

[2]*Department of Physics, Kyushu University, Fukuoka 819-0395, Japan*

[3]*Center for Quantum Information and Quantum Biology, The University of Osaka, Toyonaka 560-8531, Japan*

[4]*Center for Spintronics Research Network, Graduate School of Engineering Science, The University of Osaka, Toyonaka 560-8531, Japan*

(Received 22 September 2025; revised 6 March 2026; accepted 27 March 2026; published 16 April 2026)

In this study, we examine how orbital degrees of freedom and Majorana surface states influence the magnetic penetration depth in the superconductor UTe_2. Using a two-orbital model, we analyze pairing states belonging to the irreducible representations of the D_{2h} crystal symmetry: A_u, B_{1u}, B_{2u}, and B_{3u}. For bulk nodal states such as B_{2u}, we find that the penetration depth for screening currents along the antinodal direction and the cylindrical axis scales as T^2, in strong contrast to the conventional T^4 law. This behavior originates from quasiparticles near the point nodes contributing to the interorbital paramagnetic current. We further show that Majorana surface states can dominate the low-temperature response. The fully gapped A_u state hosts Majorana cones, which produce a T^3 dependence of the penetration depth when the ratio of penetration depth to coherence length (κ) is small. In contrast, the other pairing states exhibit Majorana Fermi arcs: The exponent is $n = 2$ along the dispersive direction, while along the dispersionless direction it depends on whether the arcs terminate at end points. The exponent $n = 2$ in the dispersive direction is robust, while it in the dispersionless direction relies on the presence or absence of the end points of the arcs and deviates from $n = 2$ when end points are absent. Our results demonstrate that penetration-depth measurements provide a direct probe of Majorana surface states in low-κ superconductors. For larger κ, the surface contribution becomes negligible and the temperature dependence is governed by bulk quasiparticles.

DOI: 10.1103/4j8h-y77j

I. INTRODUCTION

Since superconductivity was first observed in UTe_2, this heavy-fermion compound has attracted considerable interest [1–4]. It is a leading candidate for materials that host spin-triplet unconventional superconductivity. Several experimental observations support spin-triplet superconductivity, including extremely high upper critical fields in all directions [5–7] and reentrant superconductivity at high magnetic fields [5,8,9]. Furthermore, the reduction in NMR Knight shift for all directions is compatible with a fully gapped spin-triplet pairing state [10]. However, identifying the superconducting gap symmetry of UTe_2 still remains a crucial unresolved challenge, even under low magnetic fields and ambient pressure.

Possible spin-triplet pairing states in UTe_2 are classified in terms of four irreducible representations of the D_{2h} point group symmetry, the A_u, B_{1u}, B_{2u}, and B_{3u} states. Besides the gap symmetry, information about the electronic band structure is also essential for understanding the unconventional superconductivity of UTe_2. The recent observation of the de Haas–van Alphen (dHvA) oscillations supports the existence of cylindrical Fermi surfaces along the k_c direction [11]. For such Fermi surfaces, the A_u and B_{1u} states are fully gapped, while the other two states have nodal points along the k_a or k_b direction (see Fig. 2). However, the pairing symmetry suggested by recent experiments remains controversial and has yet to be established. For instance, the spontaneous breaking of time-reversal symmetry has been reported in samples with $T_c = 1.6$ K [12,13], while the recent remarkable improvement in sample quality increases the superconducting transition temperature at zero fields from $T_c = 1.6$ K to 2.1 K [14,15], and Kerr effect and zero-field muon spin relaxation measurements on high-quality samples have shown no evidence of broken time-reversal symmetry [16,17]. The nodal structures of the superconducting gap may be identified experimentally through the power-law behaviors in the temperature dependence of thermal and magnetic measurements. In another instance, thermal conductivity measurements yield conflicting results for the gap symmetries: One group indicates a fully gapped A_u state [18], while another presents data indicating the existence of point nodes [19]. Furthermore, measurements of specific heat and magnetic penetration depth indicate the presence of point nodes, suggesting a nonunitary $B_{3u} + iA_u$ state with spontaneously broken time-reversal symmetry [20]. As a result, the irreducible representation and gap symmetry have yet to be determined.

*Contact author: tei@blade.mp.es.osaka-u.ac.jp
†Contact author: fuji@mp.es.osaka-u.ac.jp
‡Contact author: mizushima@mp.es.osaka-u.ac.jp

 ©2026 American Physical Society

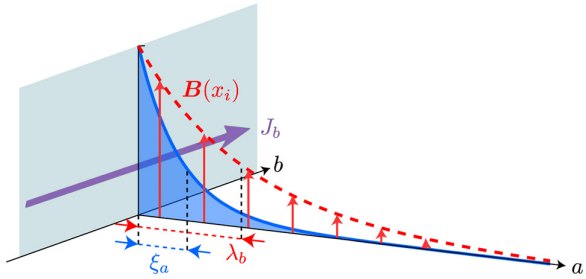


FIG. 1. An external magnetic field is screened by the superconducting current, J_b, resulting in an exponential decay of the magnetic field over the characteristic length scale of the magnetic penetration depth, λ_b. The blue curve illustrates the probability density of the Majorana surface states, which are localized within the coherence length ξ_a from the boundary.

Among several experiments, we here focus on magnetic penetration depth measurements [20–22], as shown in Fig. 1. According to the theory based on bulk gap structures [23,24], in superconductors with nodal points, the magnetic field penetration depth of the Meissner current along the nodal (antinodal) direction behaves as T^2 (T^4). Recent experiment [20] reports T^2 dependence of superfluid density in all directions, suggesting a nonunitary pairing state with point nodes. However, in the case with time-reversal symmetry, all possible pairing states in UTe_2 belong to topological phases protected by crystalline symmetries, and Majorana quasiparticles residing on the surfaces are responsible for anomalous magnetic response and tunneling phenomena [25–31]. Therefore, it is natural to consider that these surface states could influence the penetration depth. Indeed, it has been predicted that Majorana surface states lead to a T^3 power-law suppression of the superfluid mass current flowing in a narrow channel of superfluid ^{3}He-B [32,33]. In a fully gapped superconductor, which belongs to topological class DIII, the Majorana cone has been shown to be responsible for the paramagnetic effect, resulting in the T^3 dependence of magnetic penetration depth [34,35]. In UTe_2 with cylindrical Fermi surfaces, the A_u state hosts Majorana cones, while Majorana Fermi arcs protected by magnetic mirror symmetries appear on the particular surface orientations in the other pairing states [25,26,31]. It is essential to clarify how differences in the dispersion of topological surface states affect the screening current and the temperature dependence of magnetic penetration depth.

In this paper, we investigate the magnetic penetration depth in the superconductor UTe_2 with a special focus on orbital degrees of freedom and Majorana surface states. Here we use an effective model involving two orbital degrees of freedom of f electrons, which arise from two uranium atoms in a unit cell of the crystal structure. We first consider bulk nodal superconductors without surface states and find that the magnetic penetration depth of the screening current along the antinodal direction exhibits the temperature dependence of T^2, which significantly deviates from T^4 expected from conventional theory [23,24]. This anomalous exponent is attributed to the quasiparticle contributions around the point nodes to the interorbital paramagnetic current.

We demonstrate that Majorana surface states can leave clear and measurable signatures in the temperature dependence of the magnetic penetration depth when the zero-temperature penetration depth becomes comparable to the coherence length. Based on a power-counting analysis of a single-band model, we show that the exponent of the surface paramagnetic current is controlled by the dimensionality of the Majorana spectrum: A Majorana cone produces a T^3 dependence, whereas Majorana arcs generically lead to T^2. Importantly, the analysis reveals that whether the arcs terminate in the surface Brillouin zone qualitatively affects the electromagnetic response—the presence or absence of arc end points strongly modifies the exponent of the screening current along the dispersionless direction at intermediate temperatures. Using an effective tight-binding model for UTe_2, we show that these general principles account for the penetration-depth exponents of candidate odd-parity pairing states. Our results suggest that penetration-depth measurements in low-κ superconductors provide a direct route to detecting Majorana surface states, while in the large-κ limit the response is dominated by bulk quasiparticles.

The organization of this paper is as follows. In Sec. II, we review the topological superconductivity of UTe_2 and the existence of Majorana surface states. We also introduce the model Hamiltonian involving two orbital f electrons. In Sec. III, the basic formulation for magnetic penetration depth in superconductors with open boundary conditions. We present the numerical results of the magnetic penetration depth in Secs. IV and V. In Sec. IV, we clarify the effects of interorbital transitions on the penetration depth in bulk superconductors without surface states, while the effect of Majorana surface states is discussed in Sec. V. Section VI is devoted to the conclusion and discussion.

II. TOPOLOGICAL SUPERCONDUCTING STATES IN UTe_2

In this section, we introduce the basic properties of superconductivity in UTe_2 and present a model Hamiltonian that captures its essential features. We also briefly summarize the Majorana surface states. In this paper, we set $\hbar = k_B = 1$.

A. BdG Hamiltonian of UTe_2

We start with the BdG Hamiltonian,

$$\mathcal{H} = \frac{1}{2}\sum_{\boldsymbol{k},\alpha,\alpha'} \boldsymbol{c}^\dagger_{\boldsymbol{k}\alpha} H_{\mathrm{BdG}}(\boldsymbol{k}) \boldsymbol{c}_{\boldsymbol{k},\alpha'}, \tag{1}$$

where

$$H_{\mathrm{BdG}}(\boldsymbol{k}) = \begin{pmatrix} H_N(\boldsymbol{k}) & \Delta(\boldsymbol{k}) \\ \Delta^\dagger(\boldsymbol{k}) & -H_N^{\mathrm{tr}}(-\boldsymbol{k}) \end{pmatrix}. \tag{2}$$

The BdG Hamiltonian consists of a normal-state part H_N and the pair potential Δ, where A^{tr} is the transpose of a matrix A. We have also defined $\boldsymbol{c}_{\boldsymbol{k}\alpha} = (c_{\boldsymbol{k}\alpha}, c^\dagger_{-\boldsymbol{k}\alpha})^{\mathrm{tr}}$, where $c_{\boldsymbol{k}\alpha}$ and $c^\dagger_{\boldsymbol{k}\alpha}$ are the annihilation and creation operators of electrons with crystal momentum $\boldsymbol{k}$ and orbital index α, respectively.

UTe_2 belongs to the space group $Immm$ (No.71, D^{25}_{2h}) and has a body-centered orthorhombic crystal structure. Within each unit cell, two uranium atoms form dimers aligned along the c axis. Regarding the normal states, dHvA experiments have revealed two kinds of cylindrical Fermi surface—electron surfaces and hole surfaces [11,36]. Despite their

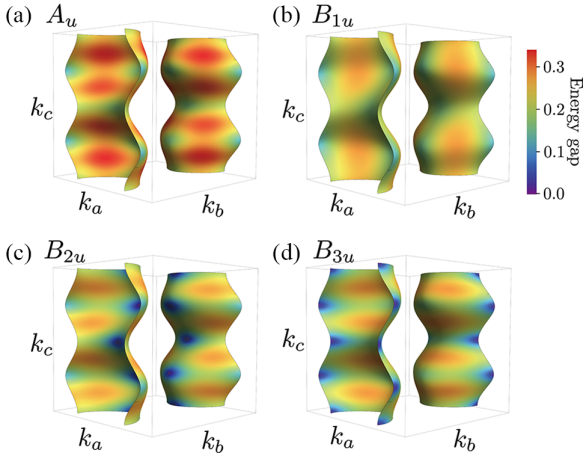


FIG. 2. Cylindrical Fermi surfaces and gap structures for (a) A_u, (b) B_{1u}, (c) B_{2u}, and (d) B_{3u} states, respectively, where $k_a a,\ k_b b \in [-\pi, \pi]$ and $k_c c \in [-2\pi, 2\pi]$. The color represents the magnitude of the superconducting gap. The A_u and B_{1u} states are fully gapped, whereas the B_{2u} and B_{3u} states have point nodes.

cylindrical shape, the observed weak anisotropy in the transport coefficients along the c axis indicates that these Fermi surfaces are quasi-2D but slightly warped along the c axis [37]. The electron sheets primarily comprise $5f$ electrons from U sites, whereas the hole sheets include $6d$ electrons at U sites and $5p$ electrons at Te sites [38,39]. Here we assume that strong Coulomb repulsion among f electrons induces magnetic fluctuations that mediate spin-triplet odd-parity pairing. To capture the Fermi surface geometry of the electron band, therefore, we adopt a simple two-orbital model that focuses only on the f electrons of the uranium dimers [25,40],

$$H_N(\boldsymbol{k}) = (\epsilon_0(\boldsymbol{k}) - \mu)\tau_0 + f_x(\boldsymbol{k})\tau_x + f_y(\boldsymbol{k})\tau_y, \tag{3}$$

where

$$\epsilon_0(\boldsymbol{k}) = 2t_1 \cos k_a a + 2t_2 \cos k_b b + 2t_3 \cos k_c c, \tag{4}$$

$$f_x(\boldsymbol{k}) = t_4 + t_5 \cos(k_a a/2)\cos(k_b b/2)\cos(k_c c/2), \tag{5}$$

$$f_y(\boldsymbol{k}) = t_6 \cos(k_a a/2)\cos(k_b b/2)\sin(k_c c/2). \tag{6}$$

Here a, b, and c are the lattice constants for each crystallographic axis and $\boldsymbol{\tau}$ is the Pauli matrix acting on the uranium-orbital space. The terms proportional to τ_0 represent intraorbital kinetic processes, while those proportional to τ_x and τ_y describe interorbital hopping. To reproduce the quasi-2D Fermi surface shown in Fig. 2, we set parameters as follows: $\mu = 2.8W$, $t_1 = 0.75W$, $t_2 = -1.0W$, $t_3 = -0.3W$, $t_4 = -1.4W$, $t_5 = 1.3W$, and $t_6 = 1.3W$, where we introduce the energy scale W, which approximately corresponds to the bandwidth. Note that this model only reproduces the electronlike Fermi surface observed in UTe_2. The holelike Fermi surfaces are obtained by rotating the electron-like Fermi surfaces by 90° around the c axis, and the effects of the holelike Fermi surfaces are considered in analogy with the results for the electronic surfaces.

Next, we consider the gap function, assuming interorbital spin-triplet Cooper pairing, which is given by

$$\Delta(\boldsymbol{k}) = \boldsymbol{d}(\boldsymbol{k}) \cdot \boldsymbol{\sigma} i\sigma_y \tau_x, \tag{7}$$

where the vectorial order parameter, $\boldsymbol{d}(\boldsymbol{k})$, characterizes the spin structure of the spin-triplet pairing and $\boldsymbol{\sigma}$ are the Pauli matrices in spin space. Here we consider only interorbital pairing states to simplify the analysis of the surface response. However, including intraorbital pairing does not alter the qualitative features of the results, such as the topological protection of the surface ABS [25]. In the point group D_{2h}, which corresponds to the space group symmetry of UTe_2, there are four possible one-dimensional irreducible representations (IRs) for odd-parity superconductivity: A_u, B_{1u}, B_{2u}, and B_{3u}. The corresponding d vector for each IR is given by

$$\boldsymbol{d}_{A_u} = \Delta_0(T)(\sin k_a a, \sin k_b b, \sin k_c c), \tag{8}$$

$$\boldsymbol{d}_{B_{1u}} = \Delta_0(T)(\sin k_b b, \sin k_a a, 0), \tag{9}$$

$$\boldsymbol{d}_{B_{2u}} = \Delta_0(T)(\sin k_c c, 0, \sin k_a a), \tag{10}$$

$$\boldsymbol{d}_{B_{3u}} = \Delta_0(T)(0, \sin k_c c, \sin k_b b). \tag{11}$$

The temperature dependence of the gap function is assumed to follow that in the BCS theory as $\Delta_0(T) = \Delta_0 \tanh(1.74\sqrt{T_c/T - 1})$ with $\Delta_0 = 0.2W$. The choice $\Delta_0 = 0.2W$ simply sets the energy scale, as the topologically protected Majorana arc dispersion is insensitive to its magnitude. We also set Δ_0 to be uniform in space. Although self-consistency would alter the gap profile near the surface over the scale of the coherence length, the low-energy structure of the Majorana surface states and the resulting power-law behavior remain unchanged.

Figure 2 illustrates the nodal structures for all IRs. Both A_u and B_{1u} are fully gapped. This is because B_{1u} has nodal points along the c axis, which opens up the Fermi surface. B_{2u} and B_{3u} are point-nodal superconductors. For cylindrical Fermi surfaces, several nodal points appear: $k_a = 0$, $k_c = 0, \pm\pi/c, \pm 2\pi/c$ in B_{2u} and $k_b = \pi/b$, $k_c = 0, \pm\pi/c, \pm 2\pi/c$ in B_{3u}. Not all nodes are necessarily protected by symmetry. In the present work, we focus on superconductors in symmetry class DIII. Owing to the coexistence of time-reversal and particle-hole symmetries, the system possesses chiral symmetry. Each nodal point is therefore protected by chiral symmetry and characterized by a topological winding number. Indeed, the nodes and the associated Majorana arcs remain stable even when additional symmetry-allowed terms are introduced, such as an orbital-singlet pairing component or higher-harmonic terms like $\sin(k_a a/2)\sin(k_b b/2)\sin(k_c c/2)$ [25,31].

B. Majorana surface states

Let us consider a slab geometry with open surfaces perpendicular to the x axis, as shown in Fig. 3(a). In this system, the BdG Hamiltonian in Eq. (2) can be recast into

$$H_{\mathrm{BdG}}^{\mathrm{lattice}}(\boldsymbol{k}_\parallel) = \begin{pmatrix} H_0(\boldsymbol{k}_\parallel) & T(\boldsymbol{k}_\parallel) & 0 & \cdots & 0 \\ T^\dagger(\boldsymbol{k}_\parallel) & H_0(\boldsymbol{k}_\parallel) & T(\boldsymbol{k}_\parallel) & \cdots & 0 \\ 0 & T^\dagger(\boldsymbol{k}_\parallel) & H_0(\boldsymbol{k}_\parallel) & \ddots & \vdots \\ \vdots & \vdots & \ddots & \ddots & T(\boldsymbol{k}_\parallel) \\ 0 & 0 & \cdots & T^\dagger(\boldsymbol{k}_\parallel) & H_0(\boldsymbol{k}_\parallel) \end{pmatrix}, \tag{12}$$

TABLE I. Summary of Majorana surface states and associated crystalline chiral operators for all IRs, where C_μ and $M_{\mu\nu}$ are the twofold rotation about the μ axis and the mirror reflection with respect to the μ-ν plane, respectively ($\mu, \nu = a, b, c$).

IR	(100)	(010)	(001)
A_u	Majorana cone Γ_{C_a}	Majorana cone Γ_{C_b}	—
B_{1u}	Flat Majorana arc $\Gamma_{M_{ca}}$	Flat Majorana arc $\Gamma_{M_{bc}}$	—
B_{2u}	Flat Majorana arc $\Gamma_{M_{ab}}$	—	Flat Majorana arc $\Gamma_{M_{bc}}$
B_{3u}	—	Flat Majorana arc $\Gamma_{M_{ab}}$	—

where $\boldsymbol{k}_\parallel$ represents the momenta parallel to the surface. The matrix is expressed in the basis of lattice sites along the x direction. The submatrices, H_0 and T, are the 8×8 matrices of the on-site Hamiltonian and the nearest-neighbor hopping terms in the spin, orbital, and Nambu bases, respectively. For simplicity, we neglect hopping processes beyond nearest neighbors.

Previous studies [25,26] examined Majorana surface states by numerically diagonalizing the BdG Hamiltonian and analyzing the associated topological invariants. When Fermi surfaces are quasi-two-dimensional and cylindrical in shape, the crystalline symmetries play crucial roles in determining the topological nature of the superconducting state. For example, using the crystalline symmetry operation U, one can define a crystalline chiral operator as

$$\Gamma_U = e^{i\phi} U \Theta C, \tag{13}$$

which enables the definition of a 1D winding number as a topological invariant. Here $e^{i\phi}$ is the phase factor chosen to satisfy the condition $\Gamma_U^2 = 1$, Θ is the time-reversal operator, and C is the particle-hole exchange operator. Table I summarizes the surface Majorana states and corresponding crystalline chiral operators for each surface and each IR. The surface states in the A_u state are protected by the twofold rotation symmetry about the surface normal axis C_μ, while flat Majorana arcs appear in the other IRs as a consequence of the mirror reflection symmetry $M_{\mu\nu}$ with respect to the μ-ν plane ($\mu, \nu = a, b, c$).

Figures 4(a) and 4(b) show the low-lying quasiparticle excitation spectra for the (010) surface of the A_u and B_{1u} states, respectively. A Majorana cone appears on the surface of the A_u state, while a Majorana arc is formed on the surface of the B_{1u} state. In the latter case, the surface state is dispersionless along the nodal direction and dispersive along the other direction in the surface Brillouin zone. The B_{2u} and B_{3u} states also exhibit Majorana arcs, similarly to those in the B_{1u} state [25,26]. We note that the bulk excitations in the B_{2u} and B_{3u} states are gapless due to the existence of nodal points on the cylindrical Fermi surfaces.

Majorana surface states are localized within the coherence length, defined in BCS theory as $\xi_i = \hbar(v_F)_i/\Delta$, $i = a, b, c$, where v_F is the Fermi velocity. In this work, we approximate the coherence length as $\xi_a/a = t_1/\Delta_0 \approx 5$, $\xi_b/b = t_2/\Delta_0 \approx 4$, and $\xi_c/c = t_3/\Delta_0 \approx 2$.

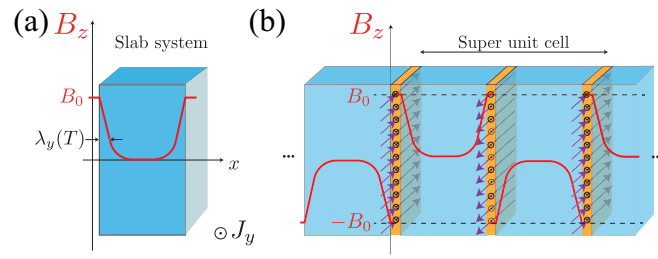


FIG. 3. (a) Slab geometry with open surfaces perpendicular to the x axis. An external magnetic field applied in the z direction is screened by a Meissner current flowing along the y axis. (b) Schematic illustration of the method of electrical mirror imaging. A planar current flowing in a thin slab reproduces the external magnetic field.

III. FORMULATION FOR MAGNETIC PENETRATION DEPTH

In this section, we describe the method for calculating the magnetic penetration depth in a tight-binding model for slab geometry with open boundary conditions. First, we calculate the current response to a static electromagnetic field using linear response theory. Then, by plugging the current response into Maxwell's equation and solving it under appropriate boundary conditions, we derive the spatial profile of the magnetic field penetrating into the superconductor.

A. Electric current response

We consider a slab geometry in Cartesian coordinates (x, y, z) with open surfaces along the x direction as shown in Fig. 3(a). The lattice constants along the x, y, and z directions are denoted by a, b, and c, respectively. The momenta parallel to the surface are denoted by $\boldsymbol{k}_\parallel = (k_y, k_z)$. The number of lattice sites along the x axis is denoted by L, with positions labeled as $x_i = 1, \ldots, L$. In the presence of an external magnetic field B_z along the z axis, a Meissner current J_y flows along the y direction to screen the magnetic field inside the superconductor. The external magnetic field is described by

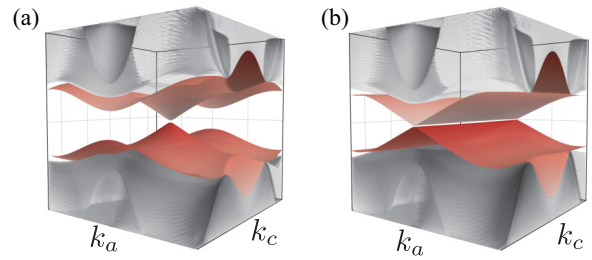


FIG. 4. (a) Typical structure of energy spectra for Majorana cone systems. The result is a slab geometry of the A_u state with open (010) surfaces. (a) Typical structure of energy spectra for Majorana Fermi arc systems. The result is a slab geometry of the B_{1u} state with open (010) surfaces.

the vector potential $A_y(x_i)$ as

$$B_z(x_i) = (A_y(x_i+1) - A_y(x_i))/a. \tag{14}$$

The vector potential couples to the Hamiltonian via minimal coupling, implemented as

$$k_y \to k_y - eA_y(x_i)/\hbar c_0, \tag{15}$$

where c_0 is the speed of light.

The current operator is defined as the functional derivative of the Hamiltonian with respect to the vector potential:

$$\hat{J}_y(x_i) = -c_0 \frac{\delta \mathcal{H}}{\delta A_y(x_i)}. \tag{16}$$

Note that the off-diagonal components in Nambu space break gauge invariance and therefore do not contribute to the current operator. To this end, we introduce the Hamiltonian that retains only the diagonal components in Nambu space.

$$\begin{aligned}\tilde{\mathcal{H}}_{\text{lattice}} = &\sum_{\boldsymbol{k}_\parallel, x_i, \alpha, \alpha'} \boldsymbol{c}^\dagger_{\boldsymbol{k}_\parallel, x_i, \alpha} [\tilde{H}_0(\boldsymbol{k}_\parallel)]_{\alpha\alpha'} \boldsymbol{c}_{\boldsymbol{k}_\parallel, x_i, \alpha'} \\ &+ \boldsymbol{c}^\dagger_{\boldsymbol{k}_\parallel, x_i, \alpha} [\tilde{T}(\boldsymbol{k}_\parallel)]_{\alpha\alpha'} \boldsymbol{c}_{\boldsymbol{k}_\parallel, x_i+1, \alpha'} + \text{H.c.},\end{aligned} \tag{17}$$

where $\tilde{H}_0(\boldsymbol{k}_\parallel)$ and $\tilde{T}(\boldsymbol{k}_\parallel)$ are the diagonal parts of onsite and nearest-neighbor BdG hopping terms in the matrix of Eq. (12), respectively. To simplify the description, we omit the orbital index from now on. We introduce the vector potential into the Hamiltonian through minimal coupling in Eq. (15) and expand the Hamiltonian to the linear order in $A_y(x_i)$. By taking the functional derivative of the resulting Hamiltonian, we express the current operator as

$$\hat{J}_y(x_i) = \hat{J}^{\text{para}}(x_i) - \frac{1}{c_0} \hat{K}^{\text{dia}}(x_i) A_y(x_i), \tag{18}$$

where $\hat{J}^{\text{para}}(x_i)$ is the paramagnetic current

$$\begin{aligned}\hat{J}^{\text{para}}(x_i) = \frac{e}{\hbar} \sum_{\boldsymbol{k}_\parallel} \Big[&\boldsymbol{c}^\dagger_{\boldsymbol{k}_\parallel, x_i} \big[\partial_{k_y} \tilde{H}_0(\boldsymbol{k}_\parallel)\big] \boldsymbol{c}_{\boldsymbol{k}_\parallel, x_i} \\ &+ \frac{1}{2} \big[\partial_{k_y} \tilde{T}(\boldsymbol{k}_\parallel)\big] \big\{ \boldsymbol{c}^\dagger_{\boldsymbol{k}_\parallel, x_i} \boldsymbol{c}_{\boldsymbol{k}_\parallel, x_i+1} + \boldsymbol{c}^\dagger_{\boldsymbol{k}_\parallel, x_i-1} \boldsymbol{c}_{\boldsymbol{k}_\parallel, x_i} \big\} \\ &+ \frac{1}{2} \big[\partial_{k_y} \tilde{T}^\dagger(\boldsymbol{k}_\parallel)\big] \big\{ \boldsymbol{c}^\dagger_{\boldsymbol{k}_\parallel, x_i+1} \boldsymbol{c}_{\boldsymbol{k}_\parallel, x_i} + \boldsymbol{c}^\dagger_{\boldsymbol{k}_\parallel, x_i} \boldsymbol{c}_{\boldsymbol{k}_\parallel, x_i-1} \big\} \Big],\end{aligned} \tag{19}$$

and $\tilde{K}^{\text{dia}}(x_i)$ is the diamagnetic kernel,

$$\begin{aligned}\hat{K}^{\text{dia}}(x_i) = -\frac{e^2}{\hbar^2} \sum_{\boldsymbol{k}_\parallel} \Big[&\boldsymbol{c}^\dagger_{\boldsymbol{k}_\parallel, x_i} \big[\partial^2_{k_y} \tilde{H}_0(\boldsymbol{k}_\parallel)\big] \boldsymbol{c}_{\boldsymbol{k}_\parallel, x_i} \\ &+ \frac{1}{2} \sum_{\boldsymbol{k}_\parallel} \big[\partial^2_{k_y} \tilde{T}(\boldsymbol{k}_\parallel)\big] \big\{ \boldsymbol{c}^\dagger_{\boldsymbol{k}_\parallel, x_i} \boldsymbol{c}_{\boldsymbol{k}_\parallel, x_i+1} + \boldsymbol{c}^\dagger_{\boldsymbol{k}_\parallel, x_i-1} \boldsymbol{c}_{\boldsymbol{k}_\parallel, x_i} \big\} \\ &+ \frac{1}{2} \sum_{\boldsymbol{k}_\parallel} \big[\partial^2_{k_y} \tilde{T}^\dagger(\boldsymbol{k}_\parallel)\big] \big\{ \boldsymbol{c}^\dagger_{\boldsymbol{k}_\parallel, x_i+1} \boldsymbol{c}_{\boldsymbol{k}_\parallel, x_i} + \boldsymbol{c}^\dagger_{\boldsymbol{k}_\parallel, x_i} \boldsymbol{c}_{\boldsymbol{k}_\parallel, x_i-1} \big\} \Big].\end{aligned} \tag{20}$$

By following the linear response theory, the expectation value of the paramagnetic current is given by

$$\big\langle \hat{J}^{\text{para}}_y(x_i) \big\rangle = -\frac{1}{c_0} \sum_{x_j} K^{\text{para}}_y(x_i, x_j) A_y(x_j), \tag{21}$$

where the paramagnetic kernel is defined as

$$\begin{aligned}K^{\text{para}}_y(x_i, x_j) = -\frac{1}{2} \sum_{\boldsymbol{k}_\parallel} \sum_{\alpha,\beta} &\frac{n_F(E_{\beta,\boldsymbol{k}_\parallel+\delta\boldsymbol{q}}) - n_F(E_{\alpha,\boldsymbol{k}_\parallel})}{E_{\beta,\boldsymbol{k}_\parallel+\delta\boldsymbol{q}} - E_{\alpha,\boldsymbol{k}_\parallel} + i\delta_\varepsilon} \\ &\times \langle u_{\beta,\boldsymbol{k}_\parallel+\delta\boldsymbol{q}} | \, \hat{J}^{\text{para}}_y(x_i) \, | u_{\alpha,\boldsymbol{k}_\parallel} \rangle \\ &\times \langle u_{\alpha,\boldsymbol{k}_\parallel} | \, \hat{J}^{\text{para}}_y(x_j) \, | u_{\beta,\boldsymbol{k}_\parallel+\delta\boldsymbol{q}} \rangle \, .\end{aligned} \tag{22}$$

Here $E^\alpha_{\boldsymbol{k}_\parallel}$ and $|u_{\alpha,\boldsymbol{k}_\parallel}\rangle$ are the eigenvalue and eigenvector of the lattice BdG Hamiltonian in Eq. (12), $H^{\text{lattice}}_{\text{BdG}}(\boldsymbol{k}_\parallel)$, labeled by the band indices α, β. The function $n_F(E) = [e^{E/T} + 1]^{-1}$ is the Fermi distribution function at temperature T. In Eq. (22), we have also introduced an infinitesimal positive constant, δ_ε. The diamagnetic kernel is given by

$$K^{\text{dia}}_y(x_i) = \frac{1}{2} \sum_{\boldsymbol{k}_\parallel, \alpha} n_F(E_{\alpha,\boldsymbol{k}_\parallel}) \, \langle u_{\alpha,\boldsymbol{k}_\parallel} | \, \hat{K}^{\text{dia}}_y(x_i) \, | u_{\alpha,\boldsymbol{k}_\parallel} \rangle \, . \tag{23}$$

B. Maxwell's equation

In order to obtain the spatial distribution of the magnetic field inside the superconductor, we solve Maxwell's equation for the vector potential $A_y(q_x)$ by employing the Fourier transformation. However, we must be cautious because the Fourier-transformed response functions, $K^{\text{para}}_y(q_x)$ and $K^{\text{dia}}_y(q_x)$, are defined in an infinite space that includes the vacuum region. To address this issue, we employ a method that introduces sheetlike source currents in an infinite medium filled with a periodic array of superconducting domains with the mirror reflected vector potential and magnetic field [41]. Figure 3(b) shows the schematic image of our setup. We first consider the superconducting domain that occupies the region $x_i = 1 \ldots L$. Then we introduce a periodic array of the mirror-reflected images of the superconducting domain. Each superconducting domain is separated by sheets through external current flows as $J^{\text{ex}}_y = \pm(c_0/2\pi)B_0$, associated with the discontinuity of the magnetic field, $2B_0$. This external current sheet is crucial to ensuring the boundary conditions, whereby the internal field matches the applied external field at the surfaces of the superconducting domain.

Maxwell's equation for the periodic array of the superconducting domain and interface with a sheet current can be solved by employing the Fourier transformation. We start to discretize Maxwell's equation in this configuration as

$$\begin{aligned}&[A_y(x_i+1) - 2A_y(x_i) + A_y(x_i-1)]/a^2 \\ &\quad = -\frac{4\pi}{c_0} \big[J^{\text{ex}}_y(x_i) + J^{\text{dia}}_y(x_i) + J^{\text{para}}_y(x_i) \big].\end{aligned} \tag{24}$$

The total current consists of three different contributions. The external current associated with the applied magnetic field B_0 is defined by

$$J^{\text{ex}}_y(x_i) = \frac{c_0}{4\pi} \sum_n \big[-2B_0 \delta_{x_i, nN} + 2B_0 \delta_{x_i, (n+1/2)N} \big], \tag{25}$$

where $N = 2L + 2$ is the number of lattice sites in one supercell. The paramagnetic current is obtained from Eq. (21) as

$$J_y^{\text{para}}(x_i) = -\frac{1}{c_0} \sum_{x_j \in \text{SC}_{x_i}} K_y^{\text{para}}(x_i, x_j) A_y(x_j). \tag{26}$$

Here SC_{x_i} denotes the set of sites within a superconducting domain. The diamagnetic current is given by

$$J_y^{\text{dia}}(x_i) = -\frac{1}{c_0} K_y^{\text{dia}}(x_i) A_y(x_i). \tag{27}$$

By employing the Fourier transformation of the discretized Maxwell's equation, we obtain

$$\frac{2}{a^2}(\cos q_x a - 1) A_y(q_x) = 2B_0(1 - e^{-iq_x N/2}) + \frac{4\pi}{c_0^2}\frac{1}{N} \sum_{q_x'} \left[K_y^{\text{para}}(q_x, -q_x') + K_y^{\text{dia}}(q_x - q_x')\right] A_y(q_x'), \tag{28}$$

where we define Fourier-transformed response functions

$$K^{\text{para}}(q_x, q_x') = \sum_{x_i, x_j = 1}^{N} e^{-iq_x x_i - iq_x' x_j} K_y^{\text{para}}(x_i, x_j), \tag{29}$$

$$K_y^{\text{dia}}(q_x) = \sum_{x_i = 1}^{N} e^{-iq_x x_i} K_y^{\text{dia}}(x_i). \tag{30}$$

Here the momentum q_x takes discrete values as $q_x = 2\pi n/N$ with $n = 1, \ldots, N$. By solving the above equation, we obtain the vector potential $A_y(q_x)$, which can be used in Eq. (14) to reconstruct the spatial profile of the magnetic field $B_z(x_i)$. The magnetic penetration depth λ_y is then defined as the spatial integral of the magnetic field from the surface to the center of the slab:

$$\lambda_y(T) = \frac{1}{B_0} \int_0^{L/2} dx\, B_z(x). \tag{31}$$

We comment on the material parameters that influence the magnitude of the magnetic penetration depth. In single-band superconductors, where the normal-state Hamiltonian consists only of Eq. (4), the paramagnetic response vanishes at zero temperature, and the diamagnetic response governs the magnetic field screening. In this model, the London penetration depth $\lambda_y^{\text{London}}$ can be defined in terms of the diamagnetic kernel as

$$\left[\lambda_y^{\text{London}}\right]^{-2} = \frac{4\pi}{c_0^2} K_y^{\text{dia}}(q_x = 0) = \frac{4\pi e^2 t_2 b^2 n}{c_0^2 \hbar^2}, \tag{32}$$

where n is the electron number density operator and t_2 is the hopping integral introduced in Eq. (4). Since the expression involves t_2, the magnitude of the magnetic penetration depth is related to the energy scale of the electronic system, with $t_2 \sim W$.

IV. EFFECT OF INTERORBITAL TRANSITIONS ON THE PENETRATION DEPTH: BULK WITHOUT SURFACE STATES

Before discussing the impact of Majorana surface states on the magnetic penetration depth, we begin by examining the behavior in the bulk without surface states. We define the penetration depth in a spatially uniform superconducting system without surfaces as

$$\lambda_{\text{Bulk}}^{-2} = \frac{4\pi}{c_0^2} K_{\text{Bulk}}(\boldsymbol{q} = \boldsymbol{0}). \tag{33}$$

The total Meissner kernel in bulk superconductors, $K_{\text{Bulk}}(\boldsymbol{q} = \boldsymbol{0})$, is composed of paramagnetic and diamagnetic contributions:

$$K_{\text{Bulk}}(\boldsymbol{q} = \boldsymbol{0}) = K_{\text{Bulk}}^{\text{para}} + K_{\text{Bulk}}^{\text{dia}}. \tag{34}$$

The paramagnetic part is given by

$$K_{\text{Bulk}}^{\text{para}} = \frac{e^2}{2\hbar^2} \sum_{\boldsymbol{k},\alpha,\beta} \frac{n_F(E_{\beta,\boldsymbol{k}}) - n_F(E_{\alpha,\boldsymbol{k}})}{E_{\beta,\boldsymbol{k}} - E_{\alpha,\boldsymbol{k}} + i\delta_\epsilon} \times \langle u_{\beta,\boldsymbol{k}} | \partial_{k_y} \tilde{H}_{\text{BdG}}(\boldsymbol{k}) | u_{\alpha,\boldsymbol{k}} \rangle \times \langle u_{\alpha,\boldsymbol{k}} | \partial_{k_y} \tilde{H}_{\text{BdG}}(\boldsymbol{k}) | u_{\beta,\boldsymbol{k}} \rangle, \tag{35}$$

while the diamagnetic part is

$$K_{\text{Bulk}}^{\text{dia}} = \frac{e^2}{2\hbar^2} \sum_{\boldsymbol{k},\alpha} n_F(E_{\alpha,\boldsymbol{k}}) \langle u_{\alpha,\boldsymbol{k}} | \partial_{k_y}^2 \tilde{H}_{\text{BdG}}(\boldsymbol{k}) | u_{\alpha,\boldsymbol{k}} \rangle. \tag{36}$$

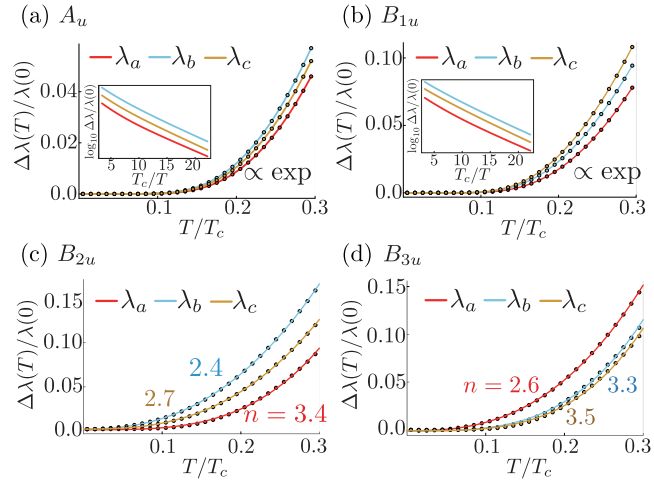


FIG. 5. Temperature dependence of magnetic penetration depth estimated from the bulk Meissner kernel. The insets in (a) and (b) show that $\log(\Delta\lambda)$ is proportional to the temperature, suggesting that exponential temperature behavior of $\Delta\lambda$. n denotes the exponent in the power-law fitting $\Delta\lambda \propto T^n$.

Figure 5 shows the temperature dependence of the magnetic penetration depth calculated from the bulk Meissner kernel for the A_u, B_{1u}, B_{2u}, and B_{3u} states, respectively. In the fully gapped A_u and B_{1u} states, the penetration depth decreases exponentially with decreasing temperature. The semilogarithmic plot of the penetration depth appears in the insets of Figs. 5(a) and 5(b), demonstrating that $\log \Delta(\lambda)$ is proportional to $1/T$.

Let us now shift our attention to the penetration depth in the nodal B_{2u} state. Figure 5(c) shows the temperature dependence of $\Delta\lambda(T) = \lambda(T) - \lambda(0)$ for currents along each spatial direction, where $\lambda(0)$ is the magnetic penetration depth at zero temperatures. In all directions, $\Delta\lambda(T)$ exhibits a

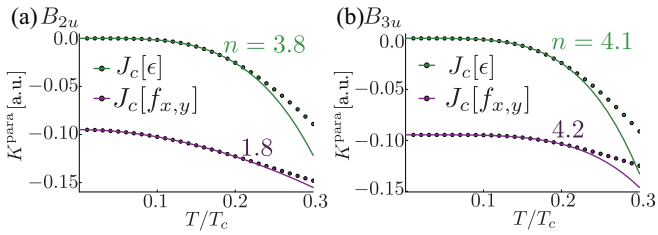


FIG. 6. Temperature dependences of paramagnetic Meissner kernel in the bulk B_{2u} state (a) and B_{3u} state (b), where $J_c[\epsilon]$ and $J_c[f_{x,y}]$ correspond to the intraorbital and interorbital components of the paramagnetic Meissner kernel. n denotes the exponent in the power-law fitting $\Delta\lambda \propto T^n$.

power-law behavior as $\Delta\lambda(T) \propto T^n$. We find that the exponents are $n = 3.4$ for λ_a, $n = 2.4$ for λ_b, and $n = 2.7$ for λ_c, indicating the presence of gapless quasiparticle excitations at the nodal points. According to conventional theory [23,24], the temperature dependence of the magnetic penetration depth in point nodal superconducting states is expected to be T^2 for the current J_b along the nodal direction, and T^4 for J_a and J_c. The exponent for λ_c, which we present in Fig. 5(c), significantly deviates from this expectation. It should be noted that the conventional theory is based on a model for single-band electrons with a spherical Fermi surface. In such a model, the B_{2u} state hosts point nodes at $k_a = k_c = 0$, and the low-energy quasiparticles carry momentum predominantly along the b axis, contributing only to J_b. In contrast, the Hamiltonian for UTe_2, which is described in Sec. II A, has a cylindrical Fermi surface and also incorporates the orbital degrees of freedom of U atoms. Below we will demonstrate that these features can lead to differences in $\Delta\lambda(T)$ compared to the conventional predictions.

The temperature dependence of the magnetic penetration depth is governed by the paramagnetic response of thermally excited quasiparticles. As shown in Eq. (35), the paramagnetic current is proportional to $\partial_{k_c} H_N$, where the current is assumed to flow along the c directions. By substituting Eq. (3) into Eq. (35), the paramagnetic current can be decomposed into two contributions: the intraorbital component $J_c[\epsilon_0(\boldsymbol{k})]$ and the interorbital components $J_c[f_x(\boldsymbol{k})]$ and $J_c[f_y(\boldsymbol{k})]$. Figure 6(a) shows the temperature dependences of the intraorbital and interorbital components of the paramagnetic kernel for J_c in the B_{2u} state. The intraorbital kernel exhibits a power-law temperature dependence of $T^{3.8}$, which is consistent with conventional expectations T^4. In contrast, the interorbital kernel shows a lower exponent of $T^{1.8}$, resulting in a significant deviation from $\Delta\lambda(T) \propto T^4$. We note that although the paramagnetic kernel also contains cross terms between $J_c[\epsilon_0(\boldsymbol{k})]$ and $J_c[f_y(\boldsymbol{k})]$, their contributions are small and negligible.

To reveal the origin of this diminished exponent in the interorbital paramagnetic response, let us now focus on the low-lying quasiparticle excitations near the nodal points at $k_a = 0$ and $k_c = 0, \pm\pi$, and discuss their contributions to the current. The intraorbital component $J_c[\epsilon_0] \propto \sin k_c$ vanishes at $k_c = 0$, implying that low-lying quasiparticles around the nodal points do not contribute to the paramagnetic response. This leads to the conventional power law, T^4, expected from a single-band model with a spherical Fermi surface. On the other hand, low-lying quasiparticle excitations near the point nodes contribute a finite amount to the interorbital paramagnetic current, as

$$J_c[f_y(\boldsymbol{k})] \propto \cos(k_a a/2)\cos(k_b b/2)\cos(k_c c/2). \tag{37}$$

Similarly, quasiparticle excitations in the vicinity of $k_a = 0$ and $k_c = \pm\pi$ have nonvanishing contributions to the interorbital current $J_c[f_x(\boldsymbol{k})]$. The contribution of quasipaticles around the nodal points via the interorbital channel deviates the power-law behavior from T^4, leading to $\Delta\lambda(T) \propto T^2$. Furthermore, the Fermi surface of UTe_2 has a quasi-2D cylindrical shape opened to the c axis, and the Fermi velocity in the c axis is vanishingly small, which also suppresses the intraorbital paramagnetic current along the c axis (J_c). As a result, for λ_c in the B_{2u} state, the interorbital paramagnetic current carried by nodal quasiparticle becomes predominant, leading to a reduced exponent of $\Delta\lambda(T)$.

Last, we discuss the magnetic penetration depth in the B_{3u} state. The nodal points are located at $k_b = \pm\pi$ on the electron Fermi surfaces; see Fig. 2(d). As shown in Fig. 5(d), the numerical results are generally consistent with conventional predictions. This implies that the contribution of the interorbital current is relatively small. As shown in Fig. 6(b), the paramagnetic kernels for both intraorbital and interorbital components of J_c exhibit the conventional power law, T^4, implying that low-energy quasiparticles do not contribute to the interorbital current. This is because the nodes in the B_{3u} state are located at $k_b = \pm\pi$, where the interorbital current component in Eq. (37) is proportional to $\cos k_b b/2$ and vanishes. This suppression is entirely accidental and stems from the simplicity of the model. In fact, UTe_2 possesses not only electron Fermi surfaces but also hole Fermi surfaces, on which the interorbital current is expected to play a more significant role.

As shown by the above discussion, the power-law exponent of the temperature dependence of the magnetic penetration depth is highly sensitive to model details, such as the shape of the Fermi surface and the presence of orbital degrees of freedom. In the following subsections, the effect of Majorana modes is defined as the deviation from the bulk behavior discussed above.

V. EFFECT OF MAJORANA SURFACE STATES ON THE PENETRATION DEPTH

In this section, we present the results of numerical calculations and analysis of magnetic penetration depths for slab geometries cleaved along crystallographic planes, (100), (010), and (001), for each IR (see Fig. 3). Figure 7 shows how the change in the magnetic penetration depth, $\Delta\lambda(T) = \lambda(T) - \lambda(0)$, from its zero-temperature value varies with temperatures for all IRs and the surfaces considered.

To maximize the effect of Majorana surface states, we first focus on the small κ regime, and the type-II limit will be discussed in Sec. V F. In Secs. V B–V E, the parameter W was chosen such that both λ_a (normalized by b or c) and λ_b (normalized by a or c) are approximately six at $T = 0$, comparable to or greater than the coherence length. These parameters correspond to the low κ regime, where κ is the GL parameter defined by $\kappa_i \equiv \lambda_i(0)/\xi_i$ ($i = a, b, c$). Due to the anisotropy of the Fermi surface—particularly the small

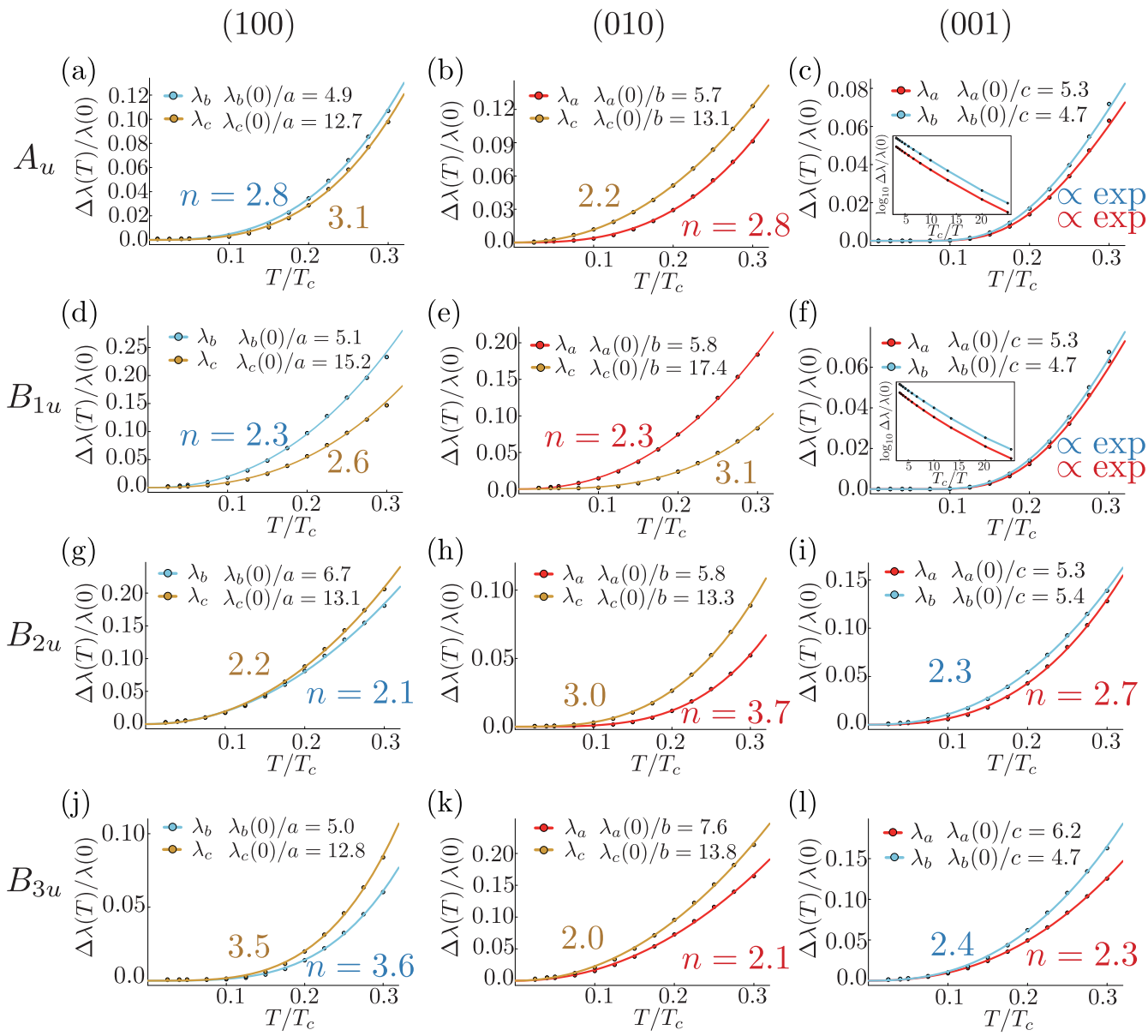


FIG. 7. Temperature dependences of the scaled magnetic penetration depth, $\Delta\lambda(T)/\lambda(0)$, for the A_u state [(a)–(c)], the B_{1u} state [(d)–(f)], the B_{2u} state [(g)–(i)], and the B_{3u} state [(j)–(l)]. The first, second, and third columns show the (100), (010), and (001) surfaces, respectively. Each curve is fitted either by a power law or an exponential function. n denotes the exponent in the power-law fitting $\Delta\lambda \propto T^n$. The insets in (c) and (f) confirm that $\Delta\lambda(T)$ is proportional to $1/T$.

dispersion along the c axis—the magnetic penetration depth is significantly longer in the c axis direction. As shown in Fig. 7, the ratio is $\lambda_c/\lambda_{a,b} \sim 2$–3.

In the following subsections, we present the results of $\Delta\lambda(T)$ for each IR in detail. Then we discuss how Majorana surface states affect the magnetic penetration depth in type-II superconductors, where the penetration depth is longer than the coherence length.

A. Impact of Majorana arcs end points on power laws

Before presenting the results for each IR, we now examine how the power-law behavior of $\Delta\lambda \propto T^n$ associated with Majorana arcs depends on the direction of the screening current and on the presence or absence of arc end points. We will show that the difference of the power-law exponent in B_{1u}, B_{2u}, and B_{3u} states are qualitatively well understandable with the flow direction and the presence or absence of Majorana arc end points in the surface Brillouin zone. Technical details of the derivation are supplemented in Appendix.

As shown in Fig. 8, we consider two typical situations of Majorana arcs: those with and without end points. The former (latter) corresponds to the surface Majorana arcs in B_{2u} and B_{3u} (B_{1u}) states. We set $k_\parallel$ and $k_\perp$ to be the momenta parallel and perpendicular to the direction of the Majorana arc, respectively.

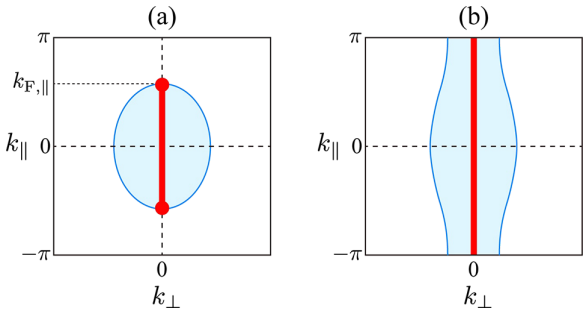


FIG. 8. Schematics of Majorana arcs (a) with and (b) without end points in the surface Brillouin zone.

The presence or absence of the Majorana arc end points has a direct impact on the temperature dependence of the magnetic penetration depth along the arc. As demonstrated in Ref. [42], when the Majorana arc terminates at well-defined end points, the phase-space restriction near the end points in the current-current correlation function leads to a robust T^2 dependence of the surface contribution, regardless of the direction and the length of the Majorana arc. Thus, the penetration depths due to the screening current flowing along $k_\perp$ and $k_\parallel$ directions exhibit the following power laws:

$$\Delta\lambda_\perp \sim T^2, \quad \Delta\lambda_\parallel \sim T^2. \tag{38}$$

However, as we discuss in Appendix, when the end points are absent and the arcs extend across the surface Brillouin zone, the exponent remains $n = 2$ in the $k_\perp$ direction, while deviating from $n = 2$ in the $k_\parallel$ direction. Therefore, the temperature dependence of the penetration depth due to Majorana arcs without end points read

$$\Delta\lambda_\perp \sim T^2, \tag{39}$$

$$\Delta\lambda_\parallel \sim aT^2 + be^{-\tilde{E}_{\min}/T}. \tag{40}$$

The characteristic energy scale is expressed by $\tilde{E}_{\min} = O(0.1\Delta)$.

In summary, the temperature dependence of the magnetic penetration depth in superconductors hosting surface Majorana arcs is given by

$$\Delta\lambda_\perp \sim T^2, \quad \Delta\lambda_\parallel \sim T^{2+\eta(T)}, \tag{41}$$

where $\eta > 0$ is not universal but depends on the material details and T. We note that $\Delta\lambda_\perp \sim T^2$ follows solely from the linear surface dispersion in the $k_\perp$ direction, and therefore remains unchanged even if the detailed shape of the Majorana arc is altered—for instance by removing the arc end points and by changing the arc length. For $\Delta\lambda_\parallel$, the additional exponent vanishes ($\eta = 0$) when the arc has end points [e.g., the (100) surface in the B_{2u} state and the (010) surface in the B_{3u} state]. When the arc end points are absent [e.g., the (100) and (010) surfaces in the B_{1u} state], the leading temperature dependence is controlled by the robust T^2 contribution, with a nonuniversal crossover near $T \sim E_{\min}$ due to the thermally activated contribution.

Using the parameters of our tight-binding model defined in Sec. II A, the characteristic temperature associated with this crossover can be estimated as $T^* \sim E_{\min} \approx 0.3T_c$. On the other hand, as discussed in the following subsections, the power of T in the numerical results is extracted by fitting the data in the temperature range $T/T_c \sim 0.1$–0.3. This interval, therefore, lies close to the crossover scale. As a result, for $\Delta\lambda_c$ in B_{1u}, the apparent temperature dependence obtained from numerical calculations deviates from the asymptotic T^2 behavior, reflecting the gradual onset of the thermally activated contribution discussed above.

B. The A_u pairing state

The A_u state hosts Majorana surface states with a cone-shaped dispersion on the (100) and (010) surfaces, while no surface states appear on the (001) surface. Figures 7(a)–7(c) show $\Delta\lambda(T)$ for each surface orientation. For the (001) surface, $\Delta\lambda_a(T)$ and $\Delta\lambda_b(T)$ exhibit an exponential decay with temperature, consistent with the bulk behavior in Sec. IV.

In contrast, the (100) and (010) surfaces show power-law temperature dependences in the penetration depth, $\Delta\lambda(T) \propto T^n$. The estimated exponents of $\Delta\lambda_{b,c}$ on the (100) surface and for $\Delta\lambda_a$ for the (010) surface are approximately $n \approx 3$ or slightly less, in good agreement with prior analytical results obtained from the continuum model for a fully gapped topological superconducting state with a Majorana cone [34]. Note that the exponent for the λ_c on the (010) surface is found to be close to $n = 2$ [see Fig. 7(b)]. As discussed in the previous subsection, the intraorbital component of the paramagnetic current response is strongly suppressed because of the quasi-2D structure of the Fermi surface. On the other hand, the interorbital paramagnetic current becomes predominant in J_c, leading to a decrease in the power-law exponent, $n < 3$.

C. The B_{1u} pairing state

The (001) surface in the B_{1u} state is topologically trivial and not accompanied by Majorana surface states. The magnetic penetration depths for this surface orientation exhibit an exponential temperature dependence, as shown in Fig. 7(f). A key difference from the A_u state is that the B_{1u} state hosts the Majorana arcs on both the (100) and (010) surfaces, which are dispersive in one direction and form a zero-energy flat-band in the other. In contrast to the cone-shaped dispersion in the A_u state, these Fermi arcs result in a large amount of surface density of states at zero energy. The quantitative difference in the density of states of the surface Majorana modes causes a change in the power-law exponent of the magnetic penetration depth, shifting from the exponent $n = 3$ for an isotropic Majorana cone.

Figure 7(d) shows the temperature dependences of $\Delta\lambda_b(T)$ and $\Delta\lambda_c(T)$ on the (100) surface. The penetration depth, $\Delta\lambda(T)$, exhibits a temperature dependence following a power law such as $\Delta\lambda_b \propto T^{2.3}$ and $\Delta\lambda_c(T) \propto T^{2.6}$. As noted in Table I, the Majorana band that forms on the (100) surface is dispersionless along the k_c direction, which is protected by the mirror reflection symmetry in the ca plane, M_{ca}. The Majorana surface state contributes less to the paramagnetic current in J_c than to J_b. As a result, the dispersionless surface states along the c axis exhibit a reduced paramagnetic contribution to the screening current, J_c, resulting in a larger exponent in $\Delta\lambda_c$ compared to $\Delta\lambda_b$. A similar feature is also observed in the magnetic responses on the (010) surface, where the

Majorana band is dispersive along k_a and flat along k_c. For this surface orientation, as shown in Fig. 7(e), $\Delta\lambda(T)$ exhibits a power-law behavior with $\Delta\lambda_a \propto T^{2.3}$ and $\Delta\lambda_c \propto T^{3.1}$. Since the B_{1u} state is fully gapped in the bulk, the low-temperature behavior is dominated by contributions from the Majorana Fermi arcs. It is important to note that the Majorana arc has no end points and extends across the surface Brillouin zone. Therefore, as discussed in Sec. V A, these results indicate that in systems with Majorana Fermi arcs, the magnetic penetration depth tends to follow a power law with an exponent of approximately $n = 2$ along the dispersive direction. In contrast, the exponent exceeds $n = 2$ in the dispersionless direction. The anisotropic magnetic response directly reflects the protection of Majorana arcs in the absence of end points.

D. The B_{2u} pairing state

The B_{2u} state hosts Majorana Fermi arc on the (100) and (001) surfaces, while no surface states appear on the (010) surface. Figures 7(g)–7(i) show the temperature dependence of $\Delta\lambda(T)$ for each of these surfaces. The (010) surface, where Majorana surface states are absent, exhibits a temperature dependence consistent with the bulk behavior as discussed in Fig. 5(c). For the (100) surface, the Majorana surface state is dispersive along the k_c direction and flat along the k_b direction. We note that the Majorana arcs appear along $k_c = 0$ and $k_c = \pm\pi$ and are terminated at finite k_b. Therefore, as mentioned in Sec. V A, the existence of the arc end points ensures the robust T^2 dependence of the magnetic penetration depth. Indeed, the power-law exponent of λ_c for the current along the dispersive direction, J_c, tends toward $n = 2$, reflecting the influence of dispersive surface states on the paramagnetic current. Although J_b flows along the dispersionless direction of the Majorana arc, the exponent of $\Delta\lambda_b$ also remains around $n = 2$, which is in contrast to $\Delta\lambda_c$ for the (100) and (010) surfaces in the fully gapped B_{1u} state with the Majorana arc. As quasiparticles near the bulk nodal poins give rise to anisotropic exponents, the isotropic T^2 behavior is attributed to the existence of the terminated Majorana arcs.

As mentioned in Table I, the (001) surface hosts the Majorana Fermi arc that is dispersive along the k_a direction and flat along the k_b direction. As shown in Fig. 7(i), although the current J_a flows along the dispersive direction of the Majorana arc state, $\Delta\lambda_a$ exhibits the temperature dependence following $T^{2.7}$. As mentioned above, the screening current along the dispersive direction of the Majorana arc commonly exhibits the exponent $n \approx 2$. However, the exponent for the (001) surface in the B_{2u} state is larger than the expected value, $n = 2$. This enhancement is likely due to additional contributions from bulk quasiparticle excitations near the point nodes, $\Delta\lambda_a^{\text{bulk}} \sim T^4$, in addition to those from the Majorana surface states.

E. The B_{3u} pairing state

The B_{3u} state hosts Majorana Fermi arcs on the (010) surface, while no Majorana surface states appear on the other surface orientations. We note that B_{2u} and B_{3u} are related by exchanging the a and b axes and therefore lead to similar physical behavior up to a relabeling of crystallographic directions, except for the (001) surface. Figures 7(j)–7(l) show the temperature dependence of $\Delta\lambda(T)$ for each of these surfaces. As the (100) surface does not host Majorana states, its penetration depth exhibits a temperature dependence similar to the bulk behavior in Fig. 5(d). The Majorana Fermi arc formed on the (010) surface is dispersive along the k_c direction but remains dispersionless along the k_a direction. Similarly with the results in the (100) surface of the B_{2u} state, the temperature dependence of the magnetic response exhibits $\Delta\lambda_a \propto T^{2.1}$ and $\Delta\lambda_c \propto T^{2.0}$ in the dispersive and dispersionless directions, respectively. These are consistent with the power-law exponent expected from the contributions of the Majorana arcs with end points.

Special attention should be paid to the result for the (001) surface. Despite the absence of Majorana surface states on this surface, the power-law exponent for $\Delta\lambda_b$, $n = 2.4$, is found to be anomalously lower than that in the bulk, $n = 3.3$ [see Fig. 7(l)]. We note that the (001) surface does not host zero-energy Majorana surface states, but it is accompanied by in-gap states, which are trivial Andreev bound states [26]. The necessary condition for nontrivial topology is the odd-parity pairing function, $\Delta(\boldsymbol{k}) = -\Delta(\underline{\boldsymbol{k}})$ with $\underline{\boldsymbol{k}} \equiv \boldsymbol{k} - 2\boldsymbol{k}(\hat{\boldsymbol{k}} \cdot \hat{\boldsymbol{n}})$, where we set $\hat{\boldsymbol{k}} = \boldsymbol{k}/|\boldsymbol{k}|$ and the unit vector normal to the surface, $\hat{\boldsymbol{n}}$. In the B_{3u} state, the gap function $d_b \propto \sin k_c$ satisfies this condition for the (001) surface. However, the topological invariant is trivial and zero-energy Majorana surface states do not exist because the cylindrical Fermi surface does not intersect the mirror-invariant plane on which the invariant is defined. Nonetheless, once a Fermi surface appears on a mirror-symmetric plane, Majorana zero-energy states appear, and it seems that a remnant of them appears in this calculation. Indeed, Ref. [26] has demonstrated that the (001) surface in the B_{3u} pairing state hosts trivial surface bound states that are absent in the bulk, and its surface density of states has a large amount of ingap states. These ingap states contribute to the anomalously lower exponent, $\Delta\lambda_b \propto T^{2.4}$.

F. Type-II limit

From the preceding discussions, we have demonstrated that Majorana surface states cause a significant change in the temperature dependence of the magnetic penetration depth when the magnetic penetration depth is comparable to the coherence length ξ. However, UTe_2 is a type-II superconductor where $\lambda(0)$ is much longer than ξ in all field directions, with $\lambda(0)$ in UTe_2 around 1 μm and approximately $\xi = O(10\,\text{nm})$ [20–22]. Let us now examine the effect of Majorana surface states in the type-II limit, $\xi \ll \lambda(0)$.

Figure 9(a) plots the temperature dependence of $\Delta\lambda_a(T)$ for the (010) surface in the A_u pairing state, for several values of $\lambda_a(0)/b$ ranging from 6 to 453 with a fixed $\xi_b/b = 4$. The inset shows how $\lambda_a(0)$ influences the power-law exponent, n, derived from the fitting of $\Delta\lambda_a(T) \propto T^n$. In the low κ regime where $\lambda(0)$ is comparable to ξ, the paramagnetic current due to the Majorana surface states dominates, leading to T^3 temperature dependence. However, as $\kappa \equiv \lambda_a(0)/\xi_b$ increases, the contributions of the surface states to the paramagnetic current weaken and the diamagnetic current relatively strengthens. As a result, the exponent of $\Delta\lambda_a(T)$ gradually intensifies and shifts towards exponential behavior, similarly to that of the

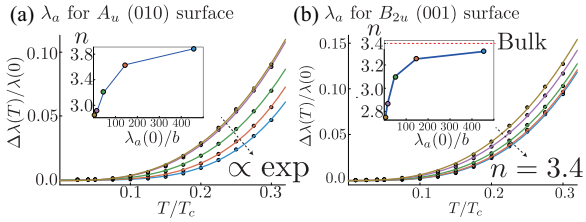


FIG. 9. (a) Temperature dependence of $\Delta\lambda_a(T)$ for the A_u state with (010) surface. (b) Temperature dependence of $\Delta\lambda_a(T)$ for the B_{2u} state with (001) surface. The insets show how the power-law exponent of the temperature dependence of $\Delta\lambda(T)$ varies with the zero-temperature value $\lambda(0)$. In the limit where the magnetic penetration depth λ is much longer than the coherence length ξ, the temperature dependence of λ approaches that of the bulk behavior.

bulk A_u state. The similar behaviors are observed in $\Delta\lambda_a(T)$ for the (001) surface in the B_{2u} state, which hosts the Majorana Fermi arc, as shown in Table I. It is seen from Fig. 9(b) that as $\lambda_a(0)/\xi_c$ increases, the exponent of $\Delta\lambda_a(T)$ approaches the value in the bulk point-nodal pairing state, $n = 3.4$. These results indicate that the contribution of Majorana surface states to the paramagnetic current becomes significant and significantly deviates from the temperature dependence of the magnetic penetration depth as $\lambda(0)$ approaches the coherence length ξ.

VI. CONCLUDING REMARKS

We have examined the effect of interorbital transitions and the impact of Majorana surface states on the temperature dependence of the magnetic penetration depths in topological superconductors. Here we focus on UTe_2 as a specific example of the topological superconductor. We start with an effective model that incorporates the orbital degrees of freedom of UTe_2 and consider the superconducting states classified in terms of four irreducible representations of the D_{2h} point group symmetry of the crystal: the A_u, B_{1u}, B_{2u}, and B_{3u} pairing states. In UTe_2 with cylindrical Fermi surfaces, the (100) and (010) surfaces of the A_u state host Majorana cones, while Majorana Fermi arcs protected by magnetic mirror symmetries appear on the particular surface orientations in the other pairing states.

First, in Sec. IV, we have discussed the interorbital effect of electrons on the magnetic penetration depth. In bulk nodal superconductors, such as the B_{2u} and B_{3u} states, the penetration depth along the antinodal direction exhibits a T^2 dependence, which significantly deviates from T^4 expected from conventional theory. This anomalous exponent is attributed to quasiparticle contributions around the point nodes to the interorbital paramagnetic current.

Furthermore, in Sec. V, we have demonstrated that when the penetration depth at $T = 0$, $\lambda(0)$, is comparable to the superconducting coherence length ξ, Majorana surface states significantly contribute to the paramagnetic current. As a result, the temperature dependence of the magnetic penetration depth deviates from that of bulk superconducting states. In a simple single-band system with an isotropic Fermi sphere, the surface contribution can be qualitatively understood from the dimensionality of the Majorana spectrum: A Majorana cone typically gives an $n = 3$ power law, whereas a Majorana arc leads to $n = 2$ in any current directions [34,42]. We have extended the arguments in Ref. [42] to the case where the Majorana arcs have no end points. The exponent in the dispersive direction is robust against the change of the arc length and the presence or absence of the arc end points. However, we have demonstrated that when the Majorana arc is terminated at momenta in the surface Brillouin zone, the exponent in the dispersionless direction deviates from $n = 2$. The presence or absence of the arc end points significantly alters the exponent of the screening current along the dispersionless direction at moderate temperatures.

Then, we have discussed the exponents of the penetration depth based on the full numerical calcualtions of the effective tight-binding model for UTe_2. In the A_u pairing state, the Majorana surface cone causes the T^3 power-law behavior of the penetration depth for both the (100) and (010) surfaces. The (100) and (010) surfaces in B_{1u} state show anisotropic magnetic responses. This is attributed to the existence of the Majorana arcs which are not terminated and extends across the surface Brillouin zone. For the (100) surface in the B_{2u} state and the (010) surface in the B_{3u} state, the existence of terminated Majorana arcs ensures the robust $n = 2$ exponent in any current directions. All these behaviors in the B_{1u}, B_{2u}, and B_{3u} states are consistent with the results obtained from the power-counting arguments in a single-band system. Therefore, in low-κ type-II superconductors, the signals of Majorana surface states may be detectable through penetration depth measurements. As κ increases and approaches the type-II limit, however, the effect of Majorana surface states on the paramagnetic current becomes weaker, and the temperature dependence of the magnetic penetration depth is governed by quasiparticle excitations in the bulk pairing states instead of surface states. In this limit, the quasiparticles around nodal points and the interorbital effect play a key role in determining the electromagnetic response.

We have not observed the nonmonotonic temperature dependences of the magnetic penetration depth, unlike the case of d-wave superconductors [43–46] and small unconventional superconductors [47,48]. In d-wave superconductors, due to the nodal line, the zero-energy flat band appears as a surface in the two-dimensional surface Brillouin zone, resulting in a prominent peak in the zero-energy density of states. In general, the zero-energy states exhibit negative superfluid density and give rise to the paramagnetic Meissner effect [49–53]. The large amount of zero-energy density of states in d-wave superconductors leads to an increase in the magnetic penetration depth with decreasing temperatures. In UTe_2, however, the possible superconducting states are either fully gapped or have point nodes, and the zero-energy states appear at a point or along a line within the surface Brillouin zone [25,26] (see also Fig. 4). As a result, the relatively small amount of zero-energy density of states in UTe_2 is insufficient to produce nonmonotonic temperature dependences, leading instead to monotonic power-law behaviors as shown in this paper.

The recent experiment in UTe_2 [20] reveals that the magnetic penetration depth exhibits a T^2 dependence in all field directions. Although topological surface states play a significant role in the electromagnetic response of topological superconductors, they cannot solely explain the anomalous

power-law behavior of the magnetic penetration depth observed in the superconductor UTe_2 with $\lambda(0)/\xi \gg 1$. Apart from the scenario of nonunitary pairing proposed in Ref. [20], a key factor in understanding the anomalous electromagnetic response is the interorbital effect of electrons. As discussed in Sec. IV, for cylindrical Fermi surfaces, the diamagnetic current flowing along the cylinder is suppressed, whereas the paramagnetic current can be enhanced by nodal quasiparticles via the interorbital process. As a result, the interorbital paramagnetic current deviates the power-law behavior from $\Delta\lambda \propto T^4$ to T^2. This interorbital effect is highly sensitive to the electron band structure in the normal state, and further study based on a more sophisticated and realistic model remains as future work.

ACKNOWLEDGMENTS

The authors are grateful to K. Ishihara and T. Shibauchi for valuable discussions from an experimental point of view. K.A. and J.T. are grateful to Y. Yamazaki for fruitful discussions. J.T. is supported by a Japan Society for the Promotion of Science (JSPS) Fellowship for Young Scientists. This work was supported by JSPS KAKENHI (Grants No. JP23K20828, No. JP23K22492, No. JP24KJ1621, No. JP25H00599, No. JP25H00609, No. JP25K07227, No. JP25K22011, and No. JP25K23361) and a Grant-in-Aid for Transformative Research Areas (A) "Correlation Design Science" (Grant No. JP25H01250) from JSPS of Japan.

DATA AVAILABILITY

The data that support the findings of this article are not publicly available upon publication because it is not technically feasible and/or the cost of preparing, depositing, and hosting the data would be prohibitive within the terms of this research project. The data are available from the authors upon reasonable request.

APPENDIX: PARAMAGNETIC KERNEL AND MAJORANA ARCS

This Appendix provides a complementary analysis of the power-law behavior of the magnetic penetration depth discussed in Sec. V A, based on the paramagnetic kernel and power-counting considerations. Let us start by considering the current-current response function $K_{\mu\nu}$. We divide it into contributions from continuum states and Majorana arc states and focus on the latter. Then the paramagnetic kernels in Eq. (22), $K^{\rm para}_{\mu\nu,ij} \equiv K^{\rm para}_{\mu\nu}(x_i, x_j)$, are given by [42]

$$K^{\rm para}_{\mu\nu,ij} \propto \int \frac{d^2\boldsymbol{k}_{\rm s}}{(2\pi)^2} J_\mu(\boldsymbol{k}_{\rm s}) J_\nu(\boldsymbol{k}_{\rm s}) \frac{\partial f(E_{\boldsymbol{k}_{\rm s}})}{\partial E_{\boldsymbol{k}_{\rm s}}} \Sigma^{\rm ss}_{ij}(\boldsymbol{k}_{\rm s}), \tag{A1}$$

where $\boldsymbol{k}_{\rm s} \equiv (k_\perp, k_\parallel)$ and $\Sigma^{\rm ss}_{ij}(\boldsymbol{k}_{\rm s}) = |\psi_{\boldsymbol{k}_{\rm s}}(x_i)|^2 |\psi_{\boldsymbol{k}_{\rm s}}(x_j)|^2$. For simplicity, we neglect the orbital degrees of freedom and consider single-band systems with normal-electron dispersion,

$$\epsilon_0(x, \boldsymbol{k}_{\rm s}) = \frac{1}{2m_0}\left[-\partial_x^2 + \alpha k_\perp^2 + \beta\cos(k_\parallel)\right] - \epsilon_F. \tag{A2}$$

The paramagnetic current operator then reduces to $\hat{J}_\mu = \partial_{k_\mu}\epsilon_0(\boldsymbol{k})$. The Majorana arc with the dispersion,

$$E_{\boldsymbol{k}_{\rm s}} = \frac{\Delta}{k_F} k_\perp, \tag{A3}$$

appears within the momentum region $\alpha k_\perp^2 + \beta\cos(k_\parallel) \leqslant k_F^2$, and the zero energy states are dispersionless along the $k_\parallel$ diretion. The wave function reads

$$\psi_{\boldsymbol{k}_{\rm s}}(x) = N_{\boldsymbol{k}_{\rm s}} e^{-x_i/l_{\rm coh}} \sinh(\kappa x), \tag{A4}$$

where we set $k_F^2 \equiv 2m_0\varepsilon_F$ and $\kappa^2 = l_{\rm coh}^{-2} + \alpha k_\perp^2 + \beta\cos(k_\parallel) - k_F^2$, and $N_{\boldsymbol{k}_{\rm s}}$ is the normalization constant.

Following Ref. [42], we expand $\Sigma^{\rm ss}_{ij}(\boldsymbol{k}_{\rm s})$ in terms of $k_\perp$ and split the kernel into two terms, $K^{\rm para}_{\mu\nu} = K^{(0)}_{\mu\nu} + K^{(2)}_{\mu\nu}$, where

$$K^{(0)}_{\mu\nu,ij} \propto \int_S \frac{d^2\boldsymbol{k}_{\rm s}}{(2\pi)^2} J_\mu(\boldsymbol{k}_{\rm s}) J_\nu(\boldsymbol{k}_{\rm s}) \frac{\partial f(E_{\boldsymbol{k}_{\rm s}})}{\partial E_{\boldsymbol{k}_{\rm s}}} \Sigma^{\rm ss}_{ij}(k_\perp = 0, k_\parallel), \tag{A5}$$

$$K^{(2)}_{\mu\nu,ij} \propto \int_S \frac{d^2\boldsymbol{k}_{\rm s}}{(2\pi)^2} J_\mu(\boldsymbol{k}_{\rm s}) J_\nu(\boldsymbol{k}_{\rm s}) \frac{\partial f(E_{\boldsymbol{k}_{\rm s}})}{\partial E_{\boldsymbol{k}_{\rm s}}} \frac{\partial^2 \Sigma^{\rm ss}_{ij}(0, k_\parallel)}{\partial^2 k_\perp} k_\perp^2, \tag{A6}$$

The $\boldsymbol{k}_{\rm s}$-integration runs over the momentum region where the surface states exist, i.e., $k_\perp \in [-g(k_\parallel), g(k_\parallel)]$ and $k_\parallel \in [-k_{F,\parallel}, k_{F,\parallel}]$. Here $k_{F,\parallel}$ satisfies $\epsilon_0(k_\perp = 0, k_\parallel = k_{F,\parallel}) = 0$, and the Fermi momentum at $k_\parallel$ is defined as $g^2(k_\parallel) = [k_F^2 - \beta\cos(k_\parallel)]/\alpha$. The Majorana arcs have end points when $k_{F,\parallel}$ is defined within the surface Brillouin zone.

Let us first consider the screening current response flowing to the $k_\perp$ direction, i.e., the dispersive direction of the Majorana arc. The dominant low-temperature power law originates from $K^{(0)}_{\mu\nu}$ with $J_\mu = J_\nu \propto k_\perp$. By performing the $k_\perp$ integration, the kernel reduces to

$$K_{\perp,ij} \approx K^{(0)}_{\perp,ij} \sim T^2, \tag{A7}$$

for $T \to 0$. The T^2 dependence is rather robust and does not rely on the presence of the Majorana arc end points. After the $k_\perp$ integration in $K^{(0)}_{\mu\nu}$, the temperature dependence arises essentially from the factor $k_\perp^2(\partial f/\partial E)$ associated with the surface dispersion $E_s = -\Delta k_\perp$. Since the derivative of the Fermi function restricts the integral to $|E_s| \sim T$, one has $|k_\perp| \sim T$, and the resulting contribution scales as $k_\perp^2 \sim T^2$. The remaining $k_\parallel$ dependence enters only through the smooth function $\Sigma^{ss}_{ij}(0, k_\parallel)$ and therefore does not modify the power law. Consequently, even if the detailed shape of the Majorana arc is altered—for instance, by removing the arc end points—the leading temperature dependence remains proportional to T^2.

We now move on to the current response along the $k_\parallel$ direction. After the $k_\parallel$ integration, the contribution $K^{(0)}_{\parallel,ij}$ can be expressed as

$$K^{(0)}_{\parallel,ij} \propto \int_0^{k_{F,\parallel}} dk_\parallel A_{ij}(k_\parallel) \tanh\left(\frac{\tilde{E}_{k_\parallel}}{2T}\right), \tag{A8}$$

where $A_{ij}(k_\parallel) \propto \sin^2(k_\parallel)\Sigma^{\rm ss}_{ij}(0, k_\parallel)$. Importantly, $A_{ij}(k_\parallel)$ is a smooth function of $k_\parallel$ and does not introduce additional

temperature dependence. We also note that the characteristic energy scale,

$$\tilde{E}(k_\parallel) = \frac{\Delta}{k_F}\sqrt{\frac{k_F^2 - \beta\cos(k_\parallel)}{\alpha}}, \tag{A9}$$

appears after the integration of the kernel $K^{(0)}_{\parallel,ij}$ over $k_\perp$. We will show below that the energy scale plays a key role in determining the temperature dependence of the kernel. Expanding the hyperbolic tangent, $\tanh(x) = 1 - 2e^{-2x} + O(e^{-4x})$, one sees that the first term gives a temperature-independent contribution, while the temperature dependence arises from

$$K^{(0)}_{\parallel,ij} \propto \text{const} + C\int_0^{k_{F,\parallel}} dk_\parallel A_{ij}(k_\parallel) e^{-\tilde{E}(k_\parallel)/T}, \tag{A10}$$

where C is the T-independent coefficient.

Let us first consider the case where the Majorana arc has end points at $k_\parallel = \pm k_{F,\parallel}$, which are defined as $\tilde{E}(k_{F,\parallel}) = 0$. In the low-temperature limit, $T \to 0$, the exponential factor, $e^{-\tilde{E}_{k_\parallel}/T}$, in $K^{(0)}_{\parallel,ij}$ strongly restricts the low-energy phase space to regions close to the arc end points. To understand the significant suppression of $K^{(0)}_{\parallel,ij}$ in the presence of the arc end points, it is useful to perform a simple power-counting analysis. Close to the arc end points, the surface dispersion behaves as $\tilde{E}(k_\parallel) \propto \delta k_\parallel$, where $k_\parallel$ is the distance from the end point. The thermally active region is determined by $E(k_z) \sim T$, implying $\delta k_\parallel \sim T^2$. The function $\Sigma_{ss}(0, k_z)$ in Eq. (A10) is proportional to $\delta k_\parallel^2$, so that within the thermally relevant region it contributes a factor of order T^4. By contrast, the current vertex varies smoothly, resulting in a temperature-independent constant. Combining these factors shows that the contribution from the end-point region is strongly suppressed at low temperatures, leading to the higher power T^6. The second contribution, $K^{(2)}_{\parallel,ij} \propto T^2$, follows directly from the $k_\perp^2(-\partial_E f)$ factor in Eq. (A6) and is largely insensitive to the detailed structure of the Majorana arc [42].

We now consider a situation in which the Majorana arc extends smoothly across the surface Brillouin zone and no arc end points are present. The characteristic energy in Eq. (A9) has a finite gap, $\tilde{E}_{\min} = \min_{k_\parallel} \tilde{E}(k_\parallel) \neq 0$, for $\forall k_\parallel$. In this case, both $A_{ij}(k_\parallel)$ and $\tilde{E}(k_\parallel)$ remain regular functions of momentum, and no special momentum point controls the $k_\parallel$ integration. The resulting temperature dependence of the kernel is given by

$$K^{\text{para}}_{\parallel,ij} \sim \text{const} + ae^{-\tilde{E}_{\min}/T} + bT^2, \tag{A11}$$

where a and b are T-independent constants. At temperatures well below this scale, $T \ll \tilde{E}_{\min}$, the exponential factor suppresses the contribution from $K^{(0)}_{\parallel,ij}$, so that the total response is dominated by

$$K^{\text{para}}_{\parallel,ij} \approx K^{(2)}_{\parallel,ij} \sim T^2. \tag{A12}$$

When the temperature becomes comparable to $\tilde{E}_{\min}$, $T \sim \tilde{E}_{\min}$ the rapid growth of $K^{(0)}_{\parallel,ij} \sim e^{-\tilde{E}_{\min}/T}$ increases the apparent power, producing an intermediate regime that can be phenomenologically described as

$$K^{\text{para}}_{\parallel,ij} \sim T^{2+\eta(T)}. \tag{A13}$$

Since this enhancement originates from a crossover rather than a singularity of the dispersion, the additional exponent, $\eta(T)$, is not universal and depends on the detailed form of $\tilde{E}(k_z)$ and T.

[1] S. Ran, C. Eckberg, Q.-P. Ding, Y. Furukawa, T. Metz, S. R. Saha, I.-L. Liu, M. Zic, H. Kim, J. Paglione, and N. P. Butch, Nearly ferromagnetic spin-triplet superconductivity, Science **365**, 684 (2019).

[2] D. Aoki, A. Nakamura, F. Honda, D. Li, Y. Homma, Y. Shimizu, Y. J. Sato, G. Knebel, J.-P. Brison, A. Pourret, D. Braithwaite, G. Lapertot, Q. Niu, M. Vališka, H. Harima, and J. Flouquet, Unconventional superconductivity in heavy fermion UTe_2, J. Phys. Soc. Jpn. **88**, 043702 (2019).

[3] D. Aoki, J.-P. Brison, J. Flouquet, K. Ishida, G. Knebel, Y. Tokunaga, and Y. Yanase, Unconventional superconductivity in UTe_2, J. Phys.: Condens. Matter **34**, 243002 (2022).

[4] S. K. Lewin, C. E. Frank, S. Ran, J. Paglione, and N. P. Butch, A review of UTe_2 at high magnetic fields, Rep. Prog. Phys. **86**, 114501 (2023).

[5] S. Ran, I.-L. Liu, Y. S. Eo, D. J. Campbell, P. M. Neves, W. T. Fuhrman, S. R. Saha, C. Eckberg, H. Kim, D. Graf, F. Balakirev, J. Singleton, J. Paglione, and N. P. Butch, Extreme magnetic field-boosted superconductivity, Nat. Phys. **15**, 1250 (2019).

[6] D. Aoki, F. Honda, G. Knebel, D. Braithwaite, A. Nakamura, D. Li, Y. Homma, Y. Shimizu, Y. J. Sato, J.-P. Brison, and J. Flouquet, Multiple superconducting phases and unusual enhancement of the upper critical field in UTe_2, J. Phys. Soc. Jpn. **89**, 053705 (2020).

[7] G. Knebel, M. Kimata, M. Vališka, F. Honda, D. Li, D. Braithwaite, G. Lapertot, W. Knafo, A. Pourret, Y. J. Sato, Y. Shimizu, T. Kihara, J.-P. Brison, J. Flouquet, and D. Aoki, Anisotropy of the upper critical field in the heavy-fermion superconductor UTe_2 under pressure, J. Phys. Soc. Jpn. **89**, 053707 (2020).

[8] A. Miyake, Y. Shimizu, Y. J. Sato, D. Li, A. Nakamura, Y. Homma, F. Honda, J. Flouquet, M. Tokunaga, and D. Aoki, Metamagnetic transition in heavy fermion superconductor UTe_2, J. Phys. Soc. Jpn. **88**, 063706 (2019).

[9] W. Knafo, M. Vališka, D. Braithwaite, G. Lapertot, G. Knebel, A. Pourret, J.-P. Brison, J. Flouquet, and D. Aoki, Magnetic-field-induced phenomena in the paramagnetic superconductor UTe_2, J. Phys. Soc. Jpn. **88**, 063705 (2019).

[10] H. Matsumura, H. Fujibayashi, K. Kinjo, S. Kitagawa, K. Ishida, Y. Tokunaga, H. Sakai, S. Kambe, A. Nakamura, Y. Shimizu, Y. Homma, D. Li, F. Honda, and D. Aoki, Large reduction in the a-axis knight shift on UTe_2 with $T_c = 2.1$ K, J. Phys. Soc. Jpn. **92**, 063701 (2023).

[11] D. Aoki, H. Sakai, P. Opletal, Y. Tokiwa, J. Ishizuka, Y. Yanase, H. Harima, A. Nakamura, D. Li, Y. Homma, Y. Shimizu, G. Knebel, J. Flouquet, and Y. Haga, First observation of the de Haas-van Alphen effect and Fermi surfaces in the unconventional superconductor UTe_2, J. Phys. Soc. Jpn. **91**, 083704 (2022).

[12] L. Jiao, S. Howard, S. Ran, Z. Wang, J. O. Rodriguez, M. Sigrist, Z. Wang, N. P. Butch, and V. Madhavan, Chiral superconductivity in heavy-fermion metal UTe_2, Nature (London) **579**, 523 (2020).

[13] I. M. Hayes, D. S. Wei, T. Metz, J. Zhang, Y. S. Eo, S. Ran, S. R. Saha, J. Collini, N. P. Butch, D. F. Agterberg, A. Kapitulnik, and J. Paglione, Multicomponent superconducting order parameter in UTe_2, Science **373**, 797 (2021).

[14] H. Sakai, P. Opletal, Y. Tokiwa, E. Yamamoto, Y. Tokunaga, S. Kambe, and Y. Haga, Single crystal growth of superconducting UTe_2 by molten salt flux method, Phys. Rev. Mater. **6**, 073401 (2022).

[15] P. F. S. Rosa, A. Weiland, S. S. Fender, B. L. Scott, F. Ronning, J. D. Thompson, E. D. Bauer, and S. M. Thomas, Single thermodynamic transition at 2 K in superconducting UTe_2 single crystals, Commun Mater **3**, 33 (2022).

[16] M. O. Ajeesh, M. Bordelon, C. Girod, S. Mishra, F. Ronning, E. D. Bauer, B. Maiorov, J. D. Thompson, P. F. S. Rosa, and S. M. Thomas, Fate of time-reversal symmetry breaking in UTe_2, Phys. Rev. X **13**, 041019 (2023).

[17] N. Azari, M. Yakovlev, N. Rye, S. R. Dunsiger, S. Sundar, M. M. Bordelon, S. M. Thomas, J. D. Thompson, P. F. S. Rosa, and J. E. Sonier, Absence of spontaneous magnetic fields due to time-reversal symmetry breaking in bulk superconducting UTe_2, Phys. Rev. Lett. **131**, 226504 (2023).

[18] S. Suetsugu, M. Shimomura, M. Kamimura, T. Asaba, H. Asaeda, Y. Kosuge, Y. Sekino, S. Ikemori, Y. Kasahara, Y. Kohsaka, M. Lee, Y. Yanase, H. Sakai, P. Opletal, Y. Tokiwa, Y. Haga, and Y. Matsuda, Fully gapped pairing state in spin-triplet superconductor UTe_2, Sci. Adv. **10**, eadk3772 (2024).

[19] I. M. Hayes, T. E. Metz, C. E. Frank, S. R. Saha, N. P. Butch, V. Mishra, P. J. Hirschfeld, and J. Paglione, Robust nodal behavior in the thermal conductivity of superconducting UTe_2, Phys. Rev. X **15**, 021029 (2025).

[20] K. Ishihara, M. Roppongi, M. Kobayashi, K. Imamura, Y. Mizukami, H. Sakai, P. Opletal, Y. Tokiwa, Y. Haga, K. Hashimoto, and T. Shibauchi, Chiral superconductivity in UTe_2 probed by anisotropic low-energy excitations, Nat. Commun. **14**, 2966 (2023).

[21] T. Metz, S. Bae, S. Ran, I.-L. Liu, Y. S. Eo, W. T. Fuhrman, D. F. Agterberg, S. M. Anlage, N. P. Butch, and J. Paglione, Point-node gap structure of the spin-triplet superconductor UTe_2, Phys. Rev. B **100**, 220504(R) (2019).

[22] S. Bae, H. Kim, Y. S. Eo, S. Ran, I.-l. Liu, W. T. Fuhrman, J. Paglione, N. P. Butch, and S. M. Anlage, Anomalous normal fluid response in a chiral superconductor UTe_2, Nat. Commun. **12**, 2644 (2021).

[23] D. Einzel, P. J. Hirschfeld, F. Gross, B. S. Chandrasekhar, K. Andres, H. R. Ott, J. Beuers, Z. Fisk, and J. L. Smith, Magnetic field penetration depth in the heavy-electron superconductor UBe_{13}, Phys. Rev. Lett. **56**, 2513 (1986).

[24] F. Gross, B. S. Chandrasekhar, D. Einzel, K. Andres, P. J. Hirschfeld, H. R. Ott, J. Beuers, Z. Fisk, and J. L. Smith, Anomalous temperature dependence of the magnetic field penetration depth in superconducting UBe_{13}, Z. Phys. B **64**, 175 (1986).

[25] J. Tei, T. Mizushima, and S. Fujimoto, Possible realization of topological crystalline superconductivity with time-reversal symmetry in UTe_2, Phys. Rev. B **107**, 144517 (2023).

[26] R. Ohashi, J. Tei, Y. Tanaka, T. Mizushima, and S. Fujimoto, Anisotropic paramagnetic response of topological Majorana surface states in the superconductor UTe_2, Phys. Rev. B **110**, 174521 (2024).

[27] H. Yoon, Y. S. Eo, J. Park, J. A. Horn, R. G. Dorman, S. R. aha, I. M. Hayes, I. Takeuchi, P. M. R. Brydon, and J. Paglione, Probing p-wave superconductivity in UTe_2 via point-contact junctions, npj Quantum Mater. **9**, 91 (2024).

[28] Z. Li, C. M. Moir, N. J. McKee, E. Lee-Wong, R. E. Baumbach, M. B. Maple, and Y. Liu, Observation of odd-parity superconductivity in UTe_2, Proc. Natl. Acad. Sci. USA **122**, e2419734122 (2025).

[29] Q. Gu, S. Wang, J. P. Carroll, K. Zhussupbekov, C. Broyles, S. Ran, N. P. Butch, J. A. Horn, S. Saha, J. Paglione, X. Liu, J. C. S. Davis, and D.-H. Lee, Pair wave function symmetry in UTe_2 from zero-energy surface state visualization, Science **388**, 938 (2025).

[30] H. Christiansen, M. Geier, B. M. Andersen, and A. Kreisel, Nodal superconducting gap structure and topological surface states of UTe_2, Phys. Rev. B **112**, 054510 (2025).

[31] J. Tei, T. Mizushima, and S. Fujimoto, Two-dimensional flat band on the $UTe_2(011)$ surface: Implication for STM measurements with a superconducting tip, Phys. Rev. B **113**, 054507 (2026).

[32] H. Wu and J. A. Sauls, Majorana excitations, spin and mass currents on the surface of topological superfluid ^{3}He-B, Phys. Rev. B **88**, 184506 (2013).

[33] J. A. Sauls, Majorana fermions as quanta of a superfluid vacuum, arXiv:2203.16698.

[34] T. C. Wu, H. K. Pal, P. Hosur, and M. S. Foster, Power-law temperature dependence of the penetration depth in a topological superconductor due to surface states, Phys. Rev. Lett. **124**, 067001 (2020).

[35] J. A. Sauls, On the excitations of a Balian–Werthamer superconductor, J. Low Temp. Phys. **208**, 87 (2022).

[36] A. Eaton, T. Weinberger, N. Popiel, Z. Wu, A. Hickey, A. Cabala, J. Pospíšil, J. Prokleška, T. Haidamak, G. Bastien, *et al.*, Quasi-2D Fermi surface in the anomalous superconductor UTe_2, Nat. Commun. **15**, 223 (2024).

[37] Y. S. Eo, S. Liu, S. R. Saha, H. Kim, S. Ran, J. A. Horn, H. Hodovanets, J. Collini, T. Metz, W. T. Fuhrman, A. H. Nevidomskyy, J. D. Denlinger, N. P. Butch, M. S. Fuhrer, L. A. Wray, and J. Paglione, c-axis transport in UTe_2: Evidence of three-dimensional conductivity component, Phys. Rev. B **106**, L060505 (2022).

[38] Y. Xu, Y. Sheng, and Y.-F. Yang, Quasi-two-dimensional Fermi surfaces and unitary spin-triplet pairing in the heavy fermion superconductor UTe_2, Phys. Rev. Lett. **123**, 217002 (2019).

[39] J. Ishizuka and Y. Yanase, Periodic Anderson model for magnetism and superconductivity in UTe_2, Phys. Rev. B **103**, 094504 (2021).

[40] T. Shishidou, H. G. Suh, P. M. R. Brydon, M. Weinert, and D. F. Agterberg, Topological band and superconductivity in UTe_2, Phys. Rev. B **103**, 104504 (2021).

[41] M. Tinkham, *Introduction to Superconductivity*, 2nd ed. (Dover, Mineola, New York, 1996).

[42] T. C. Wu, H. K. Pal, and M. S. Foster, Topological anomalous skin effect in Weyl superconductors, Phys. Rev. B **103**, 104517 (2021).

[43] S. Higashitani, Mechanism of paramagnetic Meissner effect in high-temperature superconductors, J. Phys. Soc. Jpn. **66**, 2556 (1997).

[44] H. Walter, W. Prusseit, R. Semerad, H. Kinder, W. Assmann, H. Huber, H. Burkhardt, D. Rainer, and J. A. Sauls, Low-temperature anomaly in the penetration depth of $YBa_2Cu_3O_7$ films: Evidence for Andreev bound states at surfaces, Phys. Rev. Lett. **80**, 3598 (1998).

[45] Y. Asano, A. A. Golubov, Y. V. Fominov, and Y. Tanaka, Unconventional surface impedance of a normal-metal film covering a spin-triplet superconductor due to odd-frequency Cooper pairs, Phys. Rev. Lett. **107**, 087001 (2011).

[46] Y. S. Barash, M. S. Kalenkov, and J. Kurkijärvi, Low-temperature magnetic penetration depth in *d*-wave superconductors: Zero-energy bound state and impurity effects, Phys. Rev. B **62**, 6665 (2000).

[47] S.-I. Suzuki and Y. Asano, Paramagnetic instability of small topological superconductors, Phys. Rev. B **89**, 184508 (2014).

[48] S.-I. Suzuki and Y. Asano, Effects of surface roughness on the paramagnetic response of small unconventional superconductors, Phys. Rev. B **91**, 214510 (2015).

[49] Y. Tanaka, Y. Asano, A. A. Golubov, and S. Kashiwaya, Anomalous features of the proximity effect in triplet superconductors, Phys. Rev. B **72**, 140503(R) (2005).

[50] T. Yokoyama, Y. Tanaka, and N. Nagaosa, Anomalous Meissner effect in a normal-metal–superconductor junction with a spin-active interface, Phys. Rev. Lett. **106**, 246601 (2011).

[51] Y. Tanaka, M. Sato, and N. Nagaosa, Symmetry and topology in superconductors—Odd-frequency pairing and edge states–, J. Phys. Soc. Jpn. **81**, 011013 (2012).

[52] S. Higashitani, Odd-frequency pairing effect on the superfluid density and the Pauli spin susceptibility in spatially nonuniform spin-singlet superconductors, Phys. Rev. B **89**, 184505 (2014).

[53] J. Linder and A. V. Balatsky, Odd-frequency superconductivity, Rev. Mod. Phys. **91**, 045005 (2019).